Emerin deregulation links nuclear shape instability to metastatic potential

Mariana Reis-Sobreiro[1], Jie-Fu Chen[1,†], Tatiana Novitskya[2], Sungyong You[1], Samantha Morley[1], Kenneth Steadman[1], Navjot Kaur Gill[3], Adel Eskaros[2], Mirja Rotinen[1], Chia-Yi Chu[4,5], Leland W.K. Chung[4, 5], Hisashi Tanaka[1], Wei Yang[1], Beatrice S. Knudsen[6, 7], Hsian-Rong Tseng[8], Amy C. Rowat[3], Edwin M. Posadas[4, 5], Andries Zijlstra[2, 9], Dolores Di Vizio[1], and Michael R. Freeman[1,*]

[1]Division of Cancer Biology and Therapeutics, Departments of Surgery, Biomedical Sciences and Pathology and Laboratory Medicine, Samuel Oschin Comprehensive Cancer Institute, Cedars-Sinai Medical Center, Los Angeles, CA 90048; [2]Department of Pathology, Microbiology and Immunology, Vanderbilt University, Nashville, TN 37240; [3]Department of Integrative Biology and Physiology, University of California, Los Angeles, CA 90095-7246; [4]Urologic Oncology Program/Uro-Oncology Research Laboratories, Samuel Oschin Comprehensive Center Institute, Cedars-Sinai Medical Center, Los Angeles, CA 90048; [5]Division of Hematology/Oncology, Department of Medicine, Cedars-Sinai Medical Center, Los Angeles, CA 90048; [6]Department of Biomedical Sciences, Cedars-Sinai Medical Center, Los Angeles, CA 90048; [7]Department of Pathology and Laboratory Medicine, Cedars-Sinai Medical Center, Los Angeles, CA 90048; [8]Department of Molecular and Medical Pharmacology, University of California, Los Angeles, CA 90095-1735; [9]Vanderbilt-Ingram Cancer Center, Nashville, TN 37232.

†Present address: Department of Pathology and Immunology, Washington University in St Louis School of Medicine.

* Corresponding Author.

Running title: Emerin deregulation leads to metastasis

Keywords: nuclear shape instability, emerin, metastasis, circulating tumor cells, extracellular vesicles

Abstract

Abnormalities in nuclear shape are a well-known feature of cancer, but their contribution to malignant progression remains poorly understood. Here, we show that depletion of the cytoskeletal regulator Diaphanous related formin 3 (DIAPH3), or the nuclear membrane-associated proteins lamin A/C, in prostate and breast cancer cells, induces nuclear shape instability, with a corresponding gain in malignant properties, including secretion of extracellular vesicles (EV) that contain genomic material. This transformation is characterized by a reduction and/or mislocalization of the inner nuclear membrane protein emerin. Consistent with this, depletion of emerin evokes nuclear shape instability and promotes metastasis. By visualizing emerin localization, evidence for nuclear shape instability was observed in cultured tumor cells, in experimental models of prostate cancer, in human prostate cancer tissues and in circulating tumor cells (CTCs) from patients with metastatic disease. Quantitation of emerin mislocalization discriminated cancer from benign tissue and correlated with disease progression in a prostate cancer cohort. Taken together, these results identify emerin as a mediator of nuclear shape stability in cancer and show that destabilization of emerin can promote metastasis.

Introduction

Despite many advances that have identified molecular alterations in cancer cells, nuclear structure remains the "gold standard" for cancer diagnosis (1). Histologic features such as nuclear size, shape, the number of nucleoli, and chromatin texture are considered clinically relevant, however the functional significance of these alterations in the context of disease progression remains difficult to interpret (1). Recent studies have identified nuclear envelope ruptures during cancer cell migration. Nuclear envelope blebs and breaks occur in non-mitotic, migratory cancer cells, facilitating their passage through small gaps, suggesting that stability of the nuclear envelope is important functionally in aggressive malignancies (2–4). Specific nuclear envelope proteins regulate the nuclear shape of immune cells, which are particularly migratory (5,6). Extensive nuclear deformations facilitate immune cell passage through interstitial gaps (5,7). Many similarities between immune cells and cancer cell motility have been described (8,9).

A primary mechanism of metastatic dissemination is the transient epithelial-to-mesenchymal transition (EMT) of migratory carcinoma cells. However, recent evidence has emerged showing that EMT is not necessarily a prerequisite for metastasis, suggesting that other cellular strategies may also play a role in cancer progression (10,11). Cancer cells can also exhibit an "amoeboid" migratory phenotype that resembles immune cell movement, in which the ability of cells to undergo extensive cellular deformations plays a critical role (7,9). Amoeboid phenotypes are associated with cancer progression (12). A key regulator of amoeboid behavior is the formin DIAPH3/mDia2, a cytoskeletal protein frequently deleted in metastatic breast and prostate cancer (13). DIAPH3-depleted breast and prostate cancer cells exhibit an amoeboid phenotype,

characterized by altered microtubule dynamics, increased motility, shedding of atypically large EV known as "large oncosomes," and increased metastatic potential (13–15). The molecular basis of these wide-ranging effects arising from loss of DIAPH3 has not been resolved.

In this study we show that amoeboid, DIAPH3-depleted cells, which are highly migratory and metastatic, display defects in nuclear shape, including nuclear envelope blebbing, deregulation of the nuclear envelope protein emerin, and secretion of EV that contain genomic material. Emerin depletion recapitulates these nuclear features and promotes metastasis in mouse models, suggesting that emerin deregulation can play a role in malignant transformation. In drug-resistant prostate cancer, lamin A/C, which stabilizes emerin at the nuclear envelope, is down-regulated. Quantitative analyses in patients using tissues and CTCs suggest that immunolocalization of emerin can identify tumor cells with nuclear shape instability. This study provides a direct link between nuclear instability, deregulation of emerin, and malignant potential, and identifies emerin as a clinically relevant biomarker of tumor aggressiveness.

Materials and methods

Antibodies and reagents. Emerin (4G5, Leica Biosystems, Wetzlar, Germany); β-Actin (AC-74, Sigma, St. Louis, MO); caveolin-1 (N-20, Santa Cruz Biotechnology, Dallas, TX); GAPDH (D16H11, Cell Signaling, Massachusetts, MA); p-Thr202/Tyr204-ERK-1/2 (D13.14.4E, Cell Signaling); ERK1/2 (Cell Signaling); pThr18/Ser19-MLC2 (Cell Signaling); MLC2 (Cell Signaling), lamin A/C (4C11; Cell Signaling); lamin A (Abcam, Cambridge, UK), cytokeratin-18 (SP69, Abcam); biotinylated anti-human epithelial cell

adhesion molecule (hEpCAM; R&D Systems, Minneapolis, MN); pan-cytokeratin (Life Technologies, Carlsbad, CA); pan-cytokeratin (Abcam); CD45 (BD Biosciences, San Jose, CA); CD45 (Abcam), Alexa Fluor 488-conjugated anti-rabbit (Life Technologies); Alexa Flour 555-conjugated anti-mouse (Life Technologies); Alexa 647-conjugated anti-rat (Life Technologies). 1,1'-Dioctadecyl-3,3,3',3'-Tetramethylindocarbocyanine Perchlorate (Dil, Thermo Fisher Scientific, Massachusetts, MA); Propidium Iodide (Life Technologies); Hoechst 33342 (Sigma); DAPI (Vector Laboratories, Burlingame, CA); rDNase (Life technologies); Exonuclease III (Thermo Fisher Scientific); RNase (Sigma); Piryon Y (Sigma); Crystal Violet (Becton Dickinson, Franklin Lakes, NJ); CellMask Orange (Thermo Fisher Scientific); Matrigel (Corning, New York, NY); Collagen (BD Biosciences); Cholera toxin B (Sigma).

Plasmids. Lentiviral shRNA targeting human emerin and lamin A/C and lentiviral non-targeting control vector were purchased from Dharmacon (Lafayette, CO). Emerin shRNA #1 (Oligo ID: TRCN0000083010) hairpin sequence: 5'-AAACCCAGGGCTGCCTTGGAAAAG-3'; emerin shRNA #2 (Oligo ID: TRCN0000083011) hairpin sequence: 5'- AAACCCAGGGCTGCCTTGGAAAAG-3'; lamin A/C shRNA #1 (Oligo ID: TRCN0000061836) hairpin sequence: 5'-AAACCCAGGGCTGCCTTGGAAAAG-3'; lamin A/C shRNA #2 (Oligo ID: TRCN0000061837) hairpin sequence: 5'- AAACCCAGGGCTGCCTTGGAAAAG-3'. The emerin lentiviral expression vector (Clone ID: ccsbBroad304_00501) was purchased from Dharmacon and the control vector (pLX304) was a gift from Dr. David Root (Addgene, Cambridge, MA, plasmid #25890 (16)).

Cell culture. DU145, LNCaP, PC3 and BT-549 cells were obtained from American Type Culture Collection (ATCC, Manassas, VA). HMEC and HMEC-HRAS^{V12} were a kind gift from Dr. Robert A. Weinberg (Whitehead Institute) and were maintained as previously described (13). Cell lines stably transfected with DIAPH3 shRNA, emerin shRNA and lamin A/C shRNA were maintained in DMEM (Thermo Fisher Scientific) supplemented with 10% fetal bovine serum (FBS, GE Healthcare Life Sciences, Marlborough, MA), 2 mM L-glutamine, 100 U/mL of penicillin, 100 µg/mL streptomycin and 2 µg/mL puromicyn (Thermo Fisher Scientific). HMEC cells were maintained in DMEM/F12 as previously described (13). DU145-GFP and DU145 DIAPH3-GFP were maintained in DMEM 10% FBS supplemented with 400 µg/mL G418 (Thermo Fisher Scientific) as described (13). All cell lines were authenticated by short tandem repeated profiling (Laragen), and were negative for mycoplasma. The cell lines were periodically tested with Mycoplasma Detection Kit (Lonza, Basel, Switzerland). All cell lines were used for no more than 5 passages after thawing.

Parallel microfiltration (PMF). The PMF device was assembled using polycarbonate membranes (Isopore membrane filter, EMD Millipore, Burlington, MA) of 10 µm pore diameter. Wells were loaded with 1% w/w bovine serum albumin (BSA) solution (Thermo Fisher Scientific) for 1h at 37°C, and then emptied and air dried at least 1h before each experiment. A cell suspension of 500,000 cells/mL in a final volume of 750 µL, was loaded into each well. Well-defined air pressure of 2.1 kPa was applied using a custom-built manometer and monitored using a pressure gauge (Noshok Inc., Berea,

OH). Percentage of retention was determined by collecting the sample suspension remaining in the top well and measuring the mass using a precision balance (Northeast Scale Inc., Hookset, NH). An automated cell counter (TC20, BioRad, Hercules, CA) was used to measure cell number and size distributions. This method enables simultaneous measurements of multiple samples using a uniform air pressure to drive cell suspensions through porous membranes. The relative deformability of a cell sample is quantified by the fraction of sample retained above the membrane (17).

Nuclear circularity measurements. For the analysis of nuclear circularity, cells were trypsinized and fixed with 2% paraformaldehyde (PFA). The nuclei were stained with DAPI. Images of the cells were taken at 100X using fluorescence microscopy (Eclipse 90i, Nikon, Minato, Tokyo). The nuclei were identified as DAPI-positive areas and the nuclear circularity was calculated with the morphometry package in NIS-Element software (Nikon).

Immunofluorescence (IF). Cells were grown on 15 mm microscope cover glasses stained with 1,1'-Dioctadecyl-3,3,3',3'-Tetramethylindocarbocyanine Perchlorate (Thermo Fisher Scientific) for 30min, washed, fixed with 4% PFA, permeabilized in 0.1% Triton X, blocked in 5% BSA and incubated with the primary antibody overnight at 4°C. For emerin and lamin A staining, the cells were fixed and permeabilized with methanol/acetone (1:1). Cells were then washed, incubated with the anti-mouse conjugate with fluorescein isothiocyanate FITC (Thermo Fisher Scientific) 1:1000 for 45min-1h at room temperature, further washed and mounted in cover slips with Prolongold (Thermo

Fisher Scientific). An Axioplan 2 microscope (Zeiss, Oberkochen, Germany) equipped with AxioCam was used for fluorescence imaging.

3D imaging. 3D reconstructions to allow rotation of the images were rendered with a blending software custom made by Dr. Kolja Wawrowsky (18).

Western blot. Whole-cell lysates were suspended in RIPA buffer (Thermo Fisher Scientific) supplemented with protease inhibitors (Sigma) and a phosphatase inhibitor cocktail (Thermo Fisher Scientific). Next, samples were boiled at 95^{o}C for 3min. 20-40 μg of protein (determined with Protein Assay Reagent, Thermo Scientific) were subjected to SDS-PAGE followed by immunoblotting on Polyvinylidene difluoride (PVDF) (0.45 μm, EMD Millipore) in a tank transfer unit and chemiluminescent detection (SuperSignal, Thermo Fisher Scientific).

Time-lapse microscopy. For real-time imaging movies, cells were plated in 25 mm cover slips and, after overnight attachment incubated with CellMask Orange (Invitrogen). Images were taken at 15s intervals with a Yokogawa Spinning Disk confocal system attached to a Nikon Ti-E microscope, using a 100x Pan Apo 1.4 NA objective. Images were collected with an Andor iXon 897 EMCCD camera and processed with Andor iQ software (Andor Technology, Belfast, UK).

EV-isolation. EV were isolated by differential centrifugation (SW28 rotor, Beckman, Brea, CA) from EV-free medium or serum-free medium as previously described (19).

Briefly, cells and debris were eliminated by centrifugation at 2,800 x g for 10min. The supernatant was then centrifuged at 10,000 x g for 30min to precipitate large EV. For discontinuous centrifugation gradient, 60%, 50%, 40%, 30%, 25%, 15%, 10% and 5% solutions from OptiPrep™ (60% aqueous iodixanol, Sigma) in 0.25M Sucrose/0.9 M NaCl/ 120 mM HEPES, pH 7.4 were used. The 10,000 x g pellets were mixed in the bottom layer and the following solutions carefully layered. Centrifugation was performed at 100,000 x g for 3h and 50min at 4°C. Eight individual fractions were collected, washed with PBS, and after centrifugation at 100,000 x g for 1h at 4°C, the pellet from each fraction was resuspended in either PBS or lysis buffer (19)**.**

DNA quantification in EV. EV were isolated using differential centrifugation as described above. EV were resuspended in PBS and treated with DNase I and exonuclease III for 30min at 37°C, to eliminate external DNA attached to the EV. The DNases were then inactivated by heating the sample at 75°C for 10min. EV were then treated with proteinase K (DNeasy Blood and Tissue Kit, Qiagen, Hilden, Germany) and RNase A (10 mg/mL) for 2min at room temperature. DNA isolation was performed per manufacturer's instruction (DNeasy Blood & Tissue Kit, Qiagen), and retrieved DNA then quantified using a Qubit fluorometer (Thermo Fisher Scientific).

Determination of EV membrane permeability based on DNA content. As described above, EV were pre-treated with DNases to eliminate external DNA. Next, EV were stained with 1 µg/mL PI for 30min at 37ºC and subsequently with 0.5 µg/mL Hoechst. Events between 1-10 µm were gated and analyzed by flow cytometry. The gate was

established using calibration beads as previously described (20). EV with compromised membrane integrity stained positive for both Hoechst and PI, whereas EV with intact membranes stained positive only for Hoechst.

Analysis of DNA *vs* RNA content in EV. The EV were pre-treated with DNases and RNases as described above. To measure internal DNA, EV were stained with 0.5 µg/mL of Hoechst for 30 min at 37ºC and subsequently with 0.5 µg/mL Pyronin Y (PY) which stain RNA. Events between 1-10 µm were gated and analyzed by flow cytometry. The gate was established using calibration beads as previously described (20).

Apoptosis quantification. The induction of apoptosis by TRAIL (Thermo Fisher Scientific) was evaluated using annexin V and PI double staining (FITC Annexin V/Dead cell Apoptosis kit, Invitrogen). DU145 cells ($3x10^5$) were plated in 6-well plates. Control cells and cells treated with 200 ng/mL TRAIL for 5h were collected, washed, and stained with annexin V and PI according to the manufacturer's instructions. Cells were gated by FSC-A x SSC-A to exclude debris and then by FSC-H x FSC-W following SSC-H x SSC-W to exclude cell doublets. Example of the gating strategy is shown in Supplementary Fig. 2e. Cells were analyzed using a flow cytometer and quantified using the FlowJo Sofware.

Colony assay. 1,000 cells were plated per well in 6 well plates. After 2 weeks, cells were fixed with 4% PFA for 10min at room temperature, and then stained with crystal violet

for 15min at room temperature. Wells were scanned and we quantified by ImageJ the total area occupied by the colonies, the average was represented in the figures.

Patient blood samples. Human studies were approved by and under the oversight of Cedars-Sinai Medical Center Institutional Review Board according to protocols 00030191 and 00033050, in compliance with the declaration of Helsinki. All subjects provided written informed consent for research blood donation. Patient samples were obtained from the Urologic Oncology Program and the Cedars-Sinai BioBank.

CTC enrichment using NanoVelcro chips. Venous blood was collected in acid-citrate dextrose-containing vacutainers (BD Biosciences) and processed within 4h of collection. CTCs were isolated using NanoVelcro Chips as previously described (21). Briefly, 1.0 mL of blood was subjected to standard density gradient centrifugation with Ficoll-Paque™ solution (Sigma). The peripheral mononuclear cells were harvested and incubated with a capture agent (biotinylated goat anti-hEpCAM antibody; R&D Systems). After washing carefully, the sample was loaded into the NanoVelcro Chip by an automated fluid handler, that consists of a streptavidin-coated NanoVelcro substrate and an overlaid polydimethylsiloxane chaotic mixer, at a consistent flow rate of 0.5 mL/hour. The captured cells immobilized on the NanoVelcro substrates were fixed using 2% PFA (Electron Microscopy Science, Hatfield, PA), and then subjected to immunocytochemical staining with DAPI, anti-pan cytokeratin (Life Technologies and Abcam), anti-CD45 (BD Biosciences and Abcam), anti-emerin (Leica Biosystems Novocastra), Alexa Fluor 488-conjugated anti-rabbit, and Alexa Flour 555-conjugated

anti-mouse (Life technologies), Alexa 647-conjugated anti-rat (Life technologies). Subsequent microscopic imaging was performed to identify the CTCs.

CTC imaging. NanoVelcro Chips were imaged using an upright fluorescence microscope (Eclipse 90i and Ti2 imaging systems; Nikon Inc, Melville, NY) and accompanied NIS-Element imaging software (Nikon). An automatic scan over the NanoVelcro chip was performed by the imaging system under x40 and x100 magnification with the channels corresponding to nuclear, CK, CD45, and emerin staining, respectively. CTCs were identified at x100 magnification, and individually imaged at x200 and x400 magnification for subsequent morphologic analysis.

3D CTC imaging. CTCs for 3D imaging were captured by NanoVelcro Chips as mentioned above. After fixation, the CTCs immobilized on the NanoVelcro substrates were stained with DAPI, anti-pan cytokeratin (Life Technologies and Abcam), anti-emerin (Leica Biosystems Novocastra), Cholera toxin B (Sigma), Alexa Flour 555-conjugated anti-mouse (Life Technologies), and Alexa Flour 647-conjugated anti-rat (Abcam). An automatic scan over the NanoVelcro chip was performed by the ImageXpress Ultra Confocal High-Content Analysis System (Molecular Devices, Sunnyvale, CA) under x40 and x100 magnifications. CTCs were identified at x100 magnification, and individually imaged with Z-stack confocal imaging protocol with an interval of 0.5 μm. The resulting image series were reconstructed into 3D animations using MetaMorph software (version 7.7.2.0; Molecular Devices).

Experimental metastasis. Cedars-Sinai Medical Center Institutional Animal Care and Use Committee (IACUC) approved the animal studies. 4- to 5-week old male C.B-Igh-1b/GbmsTac-Prkdcscid-Lystbg N7 SCID/Beige mice were purchased from Taconic and maintained under specific pathogen-free conditions. A total of $1x10^6$ cells were injected via intracardiac route into 6-8 week-old SCID/Beige mice. Prior to injection, the DU145 control, emerin-depleted and lamin A/C-depleted cells were transduced with luciferase-containing lentiviral particles (Genetarget Inc., San Diego, CA) and selected with 400 μg/mL here Neomycin (Thermo Fisher Scientific) for two weeks. Bioluminescence imaging was assessed weekly to monitor tumor metastasis using a Xenogen IVIS Spectrum Imaging System (PerkinElmer, Waltham, MA). Mice were sacrificed and the organs collected and fixed in 10% formalin for further histological analyses. Animals with tumor growth around the heart were excluded.

Migration and invasion assays. Boyden chambers were coated with collagen for migration assays, or with Matrigel for invasion. Briefly, 100,000 cells were resuspended in 500 μL of serum free medium and added to the upper compartment of a transwell chamber (pore size of 8.0 μm, Corning). Five hundred microliters of medium supplemented with 10% FBS were added to a 12-well plate. The transwell was placed on the plate for 12 hours (migration) or 24h (invasion). Cells were fixed and stained with crystal violet. The cells that remained in top of the chamber were discarded. The number of cells that migrated or invaded were quantified by imaging using 5 randomly chosen fields. The cell counter from ImageJ was used for quantification.

Prostate cancer tissue microarray (TMA). A prostate cancer TMA was constructed using semi-automated robotic strategy as described previously (22). TMA cores were taken from formalin fixed, paraffin embedded tissue obtained at the time of prostatectomy for patients treated at the Vanderbilt University Medical Center (2000-2012). Each patient was represented by two cores of tumor and two cores of adjacent benign tissue. Two cores of lymph node tissue were included when available. A total of 80 patients were evaluated for this study.

TMA immunofluorescent staining. A 4-6 μm section of the TMA was stained with fluorescently labeled antibody after dewaxing in xylene, rehydrating in PBS, and antigen retrieval in a boiling water bath using pH 6 citrate buffer (Dako, Carpinteria, CA) for 30min. The tissue sections were stained using a two-step cycling staining strategy, in which the first cycle included antibodies to cytokeratin 18, emerin and Histone H3. For the second cycle, a mouse anti-smooth muscle actin antibody (clone 1A4, Abcam) was used. Conventional fluorescent anti-mouse secondary antibodies were used to visualize staining with anti-cytokeratin 18 and emerin antibody. Histone H3 and smooth muscle actin were detected with antibodies enabled with photocleavable fluorescent labels. SYTOX Green (Thermo Fisher Scientific) was used to stain the nuclear DNA. Whole-slide scanning (Aperio, Vista, CA) was used to digitize the slide. Images of individual cores were extracted and processed for further analysis.

TMA quantitative analysis of emerin particles. An integrated image analysis workflow for the identification and quantitation of emerin particles was created in Konstanz Information Miner (KNIME, 10.1145/1656274.1656280, **Supplementary Fig. S1**). After images for individual fluorescent channels were loaded into the workflow (**Supplementary Fig. S1A**) and annotated (**Supplementary Fig. S1B**), the cytokeratin, nuclear and emerin images were segmented in parallel (**Supplementary Fig. S1C and S1D**). The cytokeratin images were segmented by conventional thresholding and converted to a binary mask that encompassed the prostate epithelium (Epithelial Mask). The images of the nuclear and emerin stains were segmented by Trainable Weka Segmentation. Trainable segmentation combines a collection of machine learning algorithms with a set of selected image features to produce pixel-based segmentations (10.1093/bioinformatics/btx180). In this instance, distinct models were generated for the segmentation of the nuclei and the emerin particles. Desired objects were filtered based on size. Emerin positive particles were subsequently identified (particle classification, **Supplementary Fig. S1E-F**) on the basis of their size, shape and emerin content. Segmentation models were improved through an iterative training process until ≥95 concordance was achieved with manual counting. Application of the epithelial mask was subsequently used to capture only emerin particles present within the prostate epithelium. The epithelial mask, segmented nuclei and emerin particles were mapped back to the original images for visualization and grouped (summed) by tissue to quantify the number observed in tumor and adjacent benign tissue for each patient (**Supplementary Fig. S1 G-H**).

Statistical analyses. Student's t-test (two-tailed) was used if data were normally distributed. Wilcoxon rank-sum test was performed to test differential expression of LMNA between the prostate cancer subgroups. Kaplan-Meier analysis and Cox proportional hazard regression analysis were performed to examine association between biochemical recurrence and LMNA expression. Analyses were performed with Prism 6 software (GraphPad, La Jolla, CA) and MATLAB (Mathworks Inc, Natick, MA, USA). Data were plotted as mean ± s.d.

Results

DIAPH3-depleted, amoeboid cells display irregular nuclear shapes and secrete non-apoptotic EV with nuclear material

While DIAPH3/mDia2 is well-characterized in the nucleation of actin filament polymerization (23), recent evidence suggests that DIAPH3 interacts with protein complexes at the nuclear envelope (24) and has a functional role inside the nucleus (25,26). In a previous report describing the DIAPH3 interactome (14), the nuclear envelope protein emerin was detected (**Supplementary Fig. S2A** (14)). This study was performed in DU145 prostate cancer cells. Here, and in agreement with the proteomic findings, we observed that DIAPH3 co-localizes with emerin in DU145 cells (**Supplementary Fig. S2B**). Emerin associates with the Linker of the Nucleoskeleton and Cytoskeleton Complex (LINC) and with A-type lamins, which are important components of the nucleoskeleton and mediators of nuclear structure (7,27,28). Therefore, we tested whether depletion of DIAPH3 affects nuclear shape stability. Initially, we measured the deformability of DIAPH3 shRNA-depleted cells versus shRNA-controls using parallel

microfiltration (PMF) (17). In this assay, cells are driven to deform through a membrane with 10 μm pores by applying constant pressure for a defined period. The fraction of the initial cell suspension retained on the membrane is then measured**.** DIAPH3 depletion in BT-549 and HMEC-HRAS^{V12} breast cancer cells significantly reduced the percentage of retained cells, suggesting an increase in cell deformability (**Fig. 1A and Supplementary Fig. S2C**), consistent with the amoeboid phenotype (29). DIAPH3-depleted DU145 cells, which exhibit an amoeboid phenotype (13), displayed irregular nuclear shape, as shown by a decrease in nuclear circularity (**Fig. 1B).** We also observed that DIAPH3 knockdown resulted in irregular nuclear contours, nuclear membrane blebbing and dispersion of emerin into nuclear membrane blebs and cytoplasmic particles, as seen by confocal microscopy (**Fig. 1C, Supplementary Fig. S2D-E and Supplementary Information Movie S1**). Nuclear membrane blebbing was also demonstrated by time-lapse video microscopy using the lipid affinity dye CellMask Orange, revealing that blebbing produces large vesicles that can be shed from the cells **(Fig. 1C-F and Supplementary Information Movie S2-3**). Unexpectedly, DIAPH3 depletion also decreased emerin protein in three different cell lines (**Fig. 1G**). Treatment with the proteasome inhibitor MG-132 restored emerin levels (**Supplementary Fig. S2F**), indicating that proteolytic degradation can account for some of the observed loss of emerin, consistent with prior results in fibroblasts lacking lamin A/C (30). Emerin was also detected in EV purified by gradient ultracentrifugation from the media of DIAPH3-depleted cells (**Fig. 1H**). Simultaneous detection of caveolin-1 in EV suggests these nuclear-derived vesicles are shed from the plasma membrane, consistent with the imaging results and in line with the hypothesis that nuclear shape instability allows the formation

of nuclear blebs that can be shed from the cells. Substantiating that these EV derive from the nucleus, we observed increased amounts of DNA in EV preparations from DIAPH3-depleted cells vs. controls**,** as well as an increase in non-apoptotic (membrane-impermeable) vesicles, as demonstrated by fluorometric quantitation and flow cytometry (**Fig. 1I and Supplementary Fig. S3A-B**). Shed EV from DIAPH3-depleted cells could be distinguished from apoptotic bodies (31), the formation of which was induced in control experiments with the pro-apoptotic protein TRAIL (**Supplementary Fig. S3C-D**). Despite these nuclear shape abnormalities with DIAPH3 depletion, these cells were highly proliferative as demonstrated by enhanced ability to grow in colonies (**Fig. 1J**). These findings suggest that DIAPH3 depletion promotes nuclear shape instability, as demonstrated by distortion of nuclear shape, nuclear membrane blebbing, emerin mislocalization and loss, and shedding of EV that contain DNA and emerin.

To examine whether emerin plays a role in cancer cell aggressiveness and nuclear shape instability, we enforced emerin expression in DIAPH3-depleted cells. A reported consequence of DIAPH3 knockdown in amoeboid models is hyperactivation of the ERK pathway (13). Consistent with this, we found ERK activation and motility enhanced in DU145 DIAPH3-depleted cells, but ERK activation and motility were suppressed when expression of emerin is enforced (**Fig. 2A-C**). These results suggest that emerin intersects with the ERK pathway.

Emerin downregulation recapitulates features seen with DIAPH3-loss

To further analyze the functional consequences of emerin loss, we depleted emerin from DU145, PC3, LNCaP prostate and BT-549 breast cancer cells (**Supplementary Fig.**

S4A). Emerin-depleted cells exhibited increased phosphorylation of both ERK1/2 (32) and myosin light chain (MLC2), phenocopying DIAPH3 silencing (13) (**Supplementary Fig. S4A**). Depletion of emerin also resulted in irregular nuclear shape, visualized by immunofluorescence imaging of lamin A or the lipid probe CellMask Orange (**Fig. 2D-F and Supplementary Fig. S4B-C**). Image analysis of nuclei further confirmed significantly lower circularity in emerin-depleted cells (**Fig. 2G**). The finding that emerin loss is sufficient to cause nuclear shape instability is consistent with previous results in muscular dystrophic fibroblast models (27,33). In addition to morphologic characteristics of nuclear shape instability, emerin-depleted cells exhibited higher deformability in comparison to control cells, as demonstrated by lower retention percentage in the PMF assay (**Fig. 2H**). Similar to what we observed in DIAPH3-depleted cells, emerin knockdown resulted in nuclear membrane blebbing and formation of cytosolic vesicles containing DNA (**Fig. 2D-F and Supplementary Fig. S4B-C**). We also detected significantly more extracellular DNA in EV from emerin-depleted cells (**Fig. 2I**). These EV had intact membranes, consistent with a non-apoptotic origin of the particles (**Supplementary Fig. S4D**). Along with the morphologic features indicating nuclear shape instability, emerin-depleted cells were more migratory (**Fig. 2J and Supplementary Fig. S4E**), more invasive (**Fig. 2K, Supplementary Fig. S4F**) and efficiently grew into bigger colonies (**Fig. 2L**) compared to empty vector controls. These findings suggest that emerin depletion alone is not only sufficient to cause nuclear shape instability, but also leads to the amoeboid phenotype in cancer cells, suggesting that emerin depletion could contribute to disease progression.

Emerin depletion promotes widespread metastasis in mouse models

To further test the hypothesis that nuclear shape instability induced by emerin depletion contributes to metastasis, luciferase-expressing DU145 control or emerin-depleted cells were introduced into severe combined immunodeficient (SCID) mice through intracardiac injection. At week 5 post-injection, bioluminescent imaging showed an increase and a wider distribution of luciferase activity in mice injected with emerin-depleted cells versus controls (**Fig. 3A and Supplementary Fig. S5A-B**). At necropsy we found that the number of metastatic sites was significantly higher in mice injected with emerin-depleted cells compared to controls (**Supplementary Fig. S5C**). Emerin knockdown also resulted in metastases at a greater range of organ sites (brain, lungs, adrenal glands, liver and bones) (**Fig. 3B and Supplementary Table S1)** as confirmed by gross examination, micro-CT, hematoxylin and eosin (H&E) staining, and immunohistochemistry (IHC) for cytokeratin, which is frequently used as a marker to detect metastatic cells of epithelial origin (**Fig. 3C and Supplementary Fig. S5C-D**). Taken together, these results show that emerin loss can lead to the development of widespread metastases.

Evidence of nuclear shape instability can be detected *in vivo*

The above experiments demonstrate that emerin loss leads to nuclear shape instability and increased cancer aggressiveness both *in vitro* and *in vivo*. Similar effects can result from loss of DIAPH3 (13), a protein that associates with emerin (14) (**Supplementary Fig. S2A-B**). These findings suggest a critical role for emerin and emerin-associated nuclear membrane proteins in nuclear shape stability and cancer

metastasis. *De novo* genomic alterations (mutations, deletions and amplifications) involving the emerin gene (*EMD*) are rare events (< 5%) in published prostate and breast cancer datasets (34) (**Supplementary Fig. S6A-B**). In contrast, *DIAPH3* loss has been shown to occur as a result of chromosomal deletion in 32% of prostate cancers and 46% of breast cancers (13). However, we found that *LMNA*, which encodes the emerin-anchoring proteins lamins A/C (35), is frequently downregulated in castration resistant prostate cancer (**Fig. 4A**). Using a transcriptomic classification system that divides prostate cancers into 3 subgroups (PCS1-3) (36), we observed downregulation of lamin A/C expression most frequently in the subtype with the worst prognosis, PCS1 (36) (**Fig. 4B**). Reduced lamin A/C expression also correlated with shorter biochemical recurrence-free survival (BCR) (**Fig. 4C**). These observations suggest that lamin A/C downregulation could disrupt emerin localization and lead to nuclear shape instability, as well as aggressive cancer.

To test the role of lamin A/C in emerin localization, lamin A/C was depleted in DU145 and BT-549 cells (**Supplementary Fig. S7A).** This manipulation induced emerin mislocalization and nuclear membrane blebbing (**Fig. 4D and Supplementary Fig. S7B**). Reduced lamin A/C levels also resulted in decreased nuclear circularity (**Fig. 4E**) and increased shedding of DNA-containing EV (**Fig. 4F**). We also observed enhanced migration (**Fig. 4G**) and invasion of lamin A/C-depleted cells *in vitro* (**Fig. 4H**) as well as a modest increase in metastasis *in vivo* (**Supplementary Fig. S7C-E and Supplementary Table S1**). Lamin A/C-silenced metastatic lesions exhibited emerin mislocalization, nuclear blebs, and EV-like emerin-positive structures (**Fig. 4I**). Taken together these findings indicate that lamin A/C downregulation, which is frequent in

drug-resistant prostate cancer, leads to nuclear shape instability, destabilization of emerin, and increased aggressiveness *in vitro* and *in vivo*.

Emerin deregulation is associated with aggressive disease in prostate cancer

Our findings identifying nuclear shape instability and concurrent emerin mislocalization, suggest that emerin spatial organization might be employed to identify cells with nuclear shape instability *in vivo*. Emerin-positive nuclear blebs and punctate structures are evident in high-grade human prostate cancer tissue from the Human Protein Atlas (**Supplementary Fig. S7F**). To explore the reproducibility of this finding, we performed quantitative IHC on a prostate cancer TMA (n=80) with emerin antibody. Using an integrated image analysis workflow developed in Konstanz Information Miner (KNIME) (**see methods**), we identified and quantified emerin-positive particles of the prostate epithelium (**Fig. 5A**). In normal epithelium, emerin localized to the nuclear envelope (**top row, white arrows**). In tumor epithelia, we observed a variable number of distinct emerin-positive particles (**red arrows**), which appeared as either multiple smaller puncta within a single nucleus (**middle row**) or a single large particle localized to the periphery of the nucleus (**bottom row**). Emerin particles were significantly more numerous in tumor tissue in comparison with adjacent benign epithelium (**Fig. 5B-D**), and their presence correlated with biochemical recurrence, suggesting a relationship between emerin mislocalization and aggressive disease (**Fig. 5E**).

We also tested the possibility that emerin levels and localization could be observed in CTCs, which are mediators of cancer metastasis (37). We isolated CTCs from prostate cancer patients with progressing disease using a microfluidic device (21,38) where CTCs

were defined by cytokeratin(+)/CD45(-) DAPI-positive cellular events (21). CTCs recovered from 15 patients were studied for emerin levels and localization. In CTCs, we identified nuclear membrane blebs, cytosolic emerin particles and EV-like structures that appeared tethered to the cell (**Fig. 5F**). Emerin puncta were associated with a total of 31 CTCs (n=70), the majority of which (n=28) were derived from a patient with advanced disease (**Fig. 5F-H**). In a separate analysis, we compared emerin expression levels in CTCs versus white blood cells (WBC) in the same high-power field. We found that emerin expression is significantly reduced in CTCs (n=63) compared to the same number of WBC (cytokeratin(-)/CD45(+) and DAPI-positive), which typically express low levels of emerin (6). These data suggest that CTCs derived from metastatic prostate cancer patients express lower emerin levels than WBC with highly deformable nuclei (**Fig. 5G**).

Discussion

In this study we have shown that loss or mislocalization of the inner nuclear envelope protein emerin in cancer cells leads to nuclear shape instability and an aggressive phenotype that results in more metastasis *in vivo*. Nuclear shape instability induced by emerin depletion was phenocopied by depletion of DIAPH3 or lamins A/C, suggesting that various molecular mechanisms that destabilize nuclear shape can converge on a phenotype characterized by amoeboid behavior and increased aggressiveness. Strikingly, we observed consistent features across a range of experimental settings, including experimental models, prostate cancer patient tissue and CTCs. Nuclear shape instability is associated with disruption of the nuclear envelope, nuclear blebbing, cytosolic fragments with nuclear content, and shedding of EV that

contain nuclear material. Low levels of emerin, which can arise in part by proteolytic degradation, were a common feature seen in the experimental models, including in clinical specimens (CTCs). Depletion of emerin levels by proteolytic degradation has been reported in cells containing *LMNA* mutations (30). Enforced emerin expression suppressed motility and ERK pathway activation, suggesting that depletion of emerin is a critical node in nuclear shape destabilization and amoeboid behavior.

Baarlink and colleagues (26) previously showed that DIAPH3/mDia2 has an important role regulating nuclear actin and the activity of the transcription factor SRF (serum response factor) (26). Similar functions were attributed to emerin and lamin A/C (39), suggesting a functional overlap among the proteins we focus on in our study: emerin, lamin A/C and DIAPH3/mDia2. The functional relationship among these proteins directed our attention to emerin, whose role remains poorly understood in cancer.

Formins interact with LINC complex proteins and play a key role regulating actin dynamics (40), suggesting that formin depletion might induce cytoskeletal-nucleoskeletal destabilization. Our observations demonstrate that DIAPH3 loss destabilizes the cell nucleus, consistent with depletion of lamin A/C in models of laminopathies (41).

Evidence for nuclear shape instability was obtained in human prostate cancer tissues and CTCs from prostate cancer patients. Using mouse models and *in vitro* cell studies, we have demonstrated that nuclear shape instability can result independently from loss of DIAPH3, emerin or lamin A/C. These findings suggest that nuclear shape instability is one mechanism underlying the emergence of amoeboid properties in cancer cells, and that this phenotype can be assayed in tissues and in the circulation. Beyond the

potential of emerin as a biomarker, the observation that particles that contain nuclear material can be shed from cells via nuclear blebbing provides a potential mechanistic explanation for previous reports of EV with genomic DNA cargo in the circulation of cancer patients (42–44). In support to our findings, Coban et al (45), describe the utility of using emerin IHC staining as biomarker for diagnosis and prognosis of thyroid lesions.

Collectively, these findings suggest that cancers with aggressive amoeboid features can be identified and monitored using clinically relevant methods. Studies are ongoing to determine whether evaluation of nuclear shape stability has a clinical benefit.

Acknowledgements

The authors wish to thank Dr. Kolja Wawrowsky for providing the 3D imaging software, Dr. Robert Damoiseaux for assisting with the confocal imaging of the CTCs and Dr. Wen-Chin Huang for assisting with the animal studies.

Disclosure of Potential Conflicts of Interests

Following the guidelines of the UCLA Conflict of Interest Review Committee (CIRC), Hsian-Rong Tseng discloses his financial interest in CytoLumina Technologies Corp., given his role as the founder of the company.

Following the guidelines of CSMC Conflicts of Interest (COI) policy, Edwin Posadas discloses his conflict of interest as an uncompensated advisory board member of CytoLumina Technologies Corp.

Grant support

This study was supported by the National Institutes of Health (R01 CA143777 to M.R. Freeman, R01 CA218526 to D. Di Vizio), 2P01 CA098912 (to L.W.K. Chung), the U.S Department of Defense (W81XWH-16-1-0567 to M.R. Freeman, W81XWH-16-1-0397 to D. Di Vizio, W81XWH-15-1-0473 to M. Reis-Sobreiro and PC151088 to J.-F. Chen), Ladies Auxiliary VFW Cancer Research Postdoctoral Fellowship (to S. Morley), Urology Care Foundation Research Scholar Award and Chesapeake Urology Associates Research Scholar Fund (to M. Rotinen), a NSF CAREER Award (DBI-1254185 to A.C. Rowat) and the Farber Family Foundation.

References

1. Zink D, Fischer AH, Nickerson JA. Nuclear structure in cancer cells. Nat. Rev. Cancer. 2004.4:677–87.
2. Raab M, Gentili M, de Belly H, Thiam HR, Vargas P, Jimenez AJ, et al. ESCRT III repairs nuclear envelope ruptures during cell migration to limit DNA damage and cell death. Science. 2016;352:359–62.
3. Shah P, Wolf K, Lammerding J. Bursting the Bubble – Nuclear Envelope Rupture as a Path to Genomic Instability? Trends Cell Biol. 2017.27:546–55.
4. Denais CM, Gilbert RM, Isermann P, McGregor AL, Te Lindert M, Weigelin B, et al. Nuclear envelope rupture and repair during cancer cell migration. Science. 2016;352:353–8.
5. Rowat AC, Jaalouk DE, Zwerger M, Ung WL, Eydelnant IA, Olins DE, et al. Nuclear envelope composition determines the ability of neutrophil-type cells to passage through micron-scale constrictions. J Biol Chem. 2013;288:8610–8.

6. Olins AL, Hoang T V., Zwerger M, Herrmann H, Zentgraf H, Noegel AA, et al. The LINC-less granulocyte nucleus. Eur J Cell Biol. 2009;88:203–14.

7. Friedl P, Wolf K, Lammerding J. Nuclear mechanics during cell migration. Curr. Opin. Cell Biol. 2011;23:55–64.

8. Davidson PM, Denais C, Bakshi MC, Lammerding J. Nuclear deformability constitutes a rate-limiting step during cell migration in 3-D environments. Cell Mol Bioeng. 2014;7:293–306.

9. Madsen CD, Sahai E. Cancer Dissemination--Lessons from Leukocytes. Dev Cell. 2017;19:13–26.

10. Fischer KR, Durrans A, Lee S, Sheng J, Li F, Wong STC, et al. Epithelial-to-mesenchymal transition is not required for lung metastasis but contributes to chemoresistance. Nature. 2015;527:472–6.

11. Zheng X, Carstens JL, Kim J, Scheible M, Kaye J, Sugimoto H, et al. Epithelial-to-mesenchymal transition is dispensable for metastasis but induces chemoresistance in pancreatic cancer. Nature. 2015;527:525–30.

12. Orgaz JL, Pandya P, Dalmeida R, Karagiannis P, Sanchez-Laorden B, Viros A, et al. Diverse matrix metalloproteinase functions regulate cancer amoeboid migration. Nat Commun. 2014;5:4255.

13. Hager MH, Morley S, Bielenberg DR, Gao S, Morello M, Holcomb IN, et al. DIAPH3 governs the cellular transition to the amoeboid tumour phenotype. EMBO Mol Med. 2012;4:743–60.

14. Morley S, You S, Pollan S, Choi J, Zhou B, Hager MH, et al. Regulation of microtubule dynamics by DIAPH3 influences amoeboid tumor cell mechanics and

sensitivity to taxanes. Sci Rep. 2015;5:12136.

15. Di Vizio D, Kim J, Hager MH, Morello M, Yang W, Lafargue CJ, et al. Oncosome formation in prostate cancer: Association with a region of frequent chromosomal deletion in metastatic disease. Cancer Res. 2009;69:5601–9.

16. Yang X, Boehm JS, Yang X, Salehi-Ashtiani K, Hao T, Shen Y, et al. A public genome-scale lentiviral expression library of human ORFs. Nat Methods. 2011;8:659–61.

17. Qi D, Gill NK, Santiskulvong C, Sifuentes J, Dorigo O, Rao J, et al. Screening cell mechanotype by parallel microfiltration. Sci Rep. 2015;5:17595.

18. Barcia C, Wawrowsky K, Barrett RJ, Liu C, Castro MG, Lowenstein PR. In Vivo Polarization of IFN- at Kupfer and Non-Kupfer Immunological Synapses during the Clearance of Virally Infected Brain Cells. J Immunol. 2008;180:1344–52.

19. Minciacchi VR, You S, Spinelli C, Morley S, Zandian M, Aspuria P, et al. Large oncosomes contain distinct protein cargo and represent a separate functional class of tumor-derived extracellular vesicles. Oncotarget. 2015;6:11327–41.

20. Morello M, Minciacchi VR, De Candia P, Yang J, Posadas E, Kim H, et al. Large oncosomes mediate intercellular transfer of functional microRNA. Cell Cycle. 2013;12:3526–36.

21. Chen JF, Ho H, Lichterman J, Lu YT, Zhang Y, Garcia MA, et al. Subclassification of prostate cancer circulating tumor cells by nuclear size reveals very small nuclear circulating tumor cells in patients with visceral metastases. Cancer. 2015;121:3240–51.

22. Eskaros AR, Egloff SAA, Boyd KL, Richardson JE, Hyndman ME, Zijlstra A.

Larger core size has superior technical and analytical accuracy in bladder tissue microarray. Lab Investig. Nature Publishing Group. 2017;97:335–42.

23. Copeland JW, Copeland SJ, Treisman R. Homo-oligomerization is essential for F-actin assembly by the formin family FH2 domain. J Biol Chem. 2004;279:50250–6.

24. Shao X, Kawauchi K, Shivashankar G V, Bershadsky AD. Novel localization of formin mDia2: importin β-mediated delivery to and retention at the cytoplasmic side of the nuclear envelope. Biol Open. 2015;4:1569–75.

25. Baarlink C, Grosse R. Formin' actin in the nucleus. Nucleus. 2014;5:15-20.

26. Baarlink C, Wang H, Grosse R. Nuclear actin network assembly by formins regulates the SRF coactivator MAL. Science. 2013;340:864–7.

27. Lammerding J, Hsiao J, Schulze PC, Kozlov S, Stewart CL, Lee RT. Abnormal nuclear shape and impaired mechanotransduction in emerin-deficient cells. J Cell Biol. 2005;170:781–91.

28. Meinke P, Nguyen TD, Wehnert MS. The LINC complex and human disease. Biochem Soc Trans. 2011;39:1693–7.

29. Wolf K, te Lindert M, Krause M, Alexander S, te Riet J, Willis AL, et al. Physical limits of cell migration: Control by ECM space and nuclear deformation and tuning by proteolysis and traction force. J Cell Biol. 2013;201:1069–84.

30. Muchir A, Massart C, van Engelen BG, Lammens M, Bonne G, Worman HJ. Proteasome-mediated degradation of integral inner nuclear membrane protein emerin in fibroblasts lacking A-type lamins. Biochem Biophys Res Commun. 2006;351:1011–7.

31. Wickman GR, Julian L, Mardilovich K, Schumacher S, Munro J, Rath N, et al. Blebs produced by actin-myosin contraction during apoptosis release damage-associated molecular pattern proteins before secondary necrosis occurs. Cell Death Differ. 2013;20:1293–305.

32. Muchir A, Wu W, Worman HJ. Reduced expression of A-type lamins and emerin activates extracellular signal-regulated kinase in cultured cells. Biochim Biophys Acta. 2009;1792:75-81.

33. Rowat AC, Lammerding J, Ipsen JH. Mechanical properties of the cell nucleus and the effect of emerin deficiency. Biophys J. 2006;91:4649–64.

34. Gao J, Aksoy BA, Dogrusoz U, Dresdner G, Gross B, Sumer SO, et al. Integrative analysis of complex cancer genomics and clinical profiles using the cBioPortal. Sci Signal. 2013;6:pl1.

35. Wu D, Flannery AR, Cai H, Ko E, Cao K. Nuclear localization signal deletion mutants of lamin A and progerin reveal insights into lamin A processing and emerin targeting. Nucleus. 2014;5:66–74.

36. You S, Knudsen BS, Erho N, Alshalalfa M, Takhar M, Ashab HAD, et al. Integrated classification of prostate cancer reveals a novel luminal subtype with poor outcome. Cancer Res. 2016;76:4948–58.

37. Massagué J, Obenauf AC. Metastatic colonization by circulating tumour cells. Nature. 2016;529:298–306.

38. Chen J-F, Lu Y-T, Cheng S, Tseng H-R, Figlin RA, Posadas EM. Circulating tumor cells in prostate cancer: beyond enumeration. Clin Adv Hematol Oncol. 2017;15:63–73.

39. Ho CY, Jaalouk DE, Vartiainen MK, Lammerding J. Lamin A/C and emerin regulate MKL1-SRF activity by modulating actin dynamics.Nature. 2013;497:507–13.

40. Kutscheidt S, Zhu R, Antoku S, Luxton GWG, Stagljar I, Fackler OT, et al. FHOD1 interaction with nesprin-2G mediates TAN line formation and nuclear movement. Nat Cell Biol. 2014;16:708-15.

41. Schreiber KH, Kennedy BK. When lamins go bad: Nuclear structure and disease. Cell. 2013;152:1365-75.

42. Balaj L, Lessard R, Dai L, Cho YJ, Pomeroy SL, Breakefield XO, et al. Tumour microvesicles contain retrotransposon elements and amplified oncogene sequences. Nat Commun. 2011;2:180.

43. Lázaro-Ibáñez E, Sanz-Garcia A, Visakorpi T, Escobedo-Lucea C, Siljander P, Ayuso-Sacido A, et al. Different gDNA content in the subpopulations of prostate cancer extracellular vesicles: Apoptotic bodies, microvesicles, and exosomes. Prostate. 2014;74:1379–90.

44. Thakur BK, Zhang H, Becker A, Matei I, Huang Y, Costa-Silva B, et al. Double-stranded DNA in exosomes: A novel biomarker in cancer detection. Cell Res. 2014;24:766–9.

45. Coban I, Cakir A, Unal TDK, Bassullu N, Karpuz V, Dogusoy GB, et al. Emerin Expression in Well Differentiated Epithelial Lesions of Thyroid: Implications in Papillary Thyroid Carcinoma Diagnosis and Predicting Malignant Behavior. Pathol Oncol Res. 2015;21:357-66.

Figure legends

Figure 1. DIAPH3-loss induces emerin mislocalization and nuclear shape instability. **A,** Percentage retention of BT-549 control or DIAPH3-depleted cells subjected to PMF. Percent retention refers to cells remaining on a 10 μm pore membrane after being subjected to 0.3 psi pressure for 30s (17). **B,** Quantification of nuclear circularity in DU145 control or DIAPH3-depleted cells (perfect circle=1; <1 represents departure from circularity). **C,** Confocal 3D images of BT-549 control or DIAPH3-depleted cells. DNA (Hoechst, blue), emerin (FITC, green) and membrane (1,1'-Dioctadecyl-3,3,3',3'-Tetramethylindocarbocyanine Perchlorate, Dil, red) staining are shown (scale bar 10 μm). **D,** DU145 DIAPH3-depleted cells shed EV. Cells were stained with the fluorescent lipid affinity dye CellMask Orange (**Supplementary Information Movie S3)**. **E,** Images of BT-549 control or DIAPH3-depleted cells using 3D reconstruction software (18) (**Supplementary information Movie S1**), note nuclear membrane blebs in DIAPH3-depleted cells. **F,** DU145 control or DIAPH3-depleted cell membranes were stained with the fluorescent lipid affinity dye CellMask Orange, arrows point to nuclear membrane blebs (**Supplementary Information Movie S2**). **G,** DIAPH3-depleted cells express lower emerin protein levels compared to control cells. Representative immunoblot (top) and quantification (bottom) of emerin levels in HMEC-HRAS^{V12}-control, BT-549-control, DU145-control or DIAPH3-depleted cells (n=4). **H,** Immunoblot showing emerin levels in secreted EV from BT-549 control or BT-549 DIAPH3-depleted cells cultured for 24h in EV-free complete culture medium. EV were purified by iodixanol buoyant density gradient and normalized to cell number. **I,** DU145 DIAPH3-depleted cells shed EV containing DNA. DNA enclosed in EV collected from culture medium

after 24h in EV-free complete culture medium from DU145 control or DIAPH3-depleted cells. DNA concentration was quantified by Qubit and the number of EV was normalized to the number of cells. **J,** Quantification of colonies in DU145 control or DU145 DIAPH3-depleted cells by ImageJ. Graphs show mean ± s.d. *P<0.05, **P<0.01, ***P<0.001. Unpaired t-test.

Figure 2. Emerin depletion induces nuclear shape instability and increases cancer cell aggressiveness *in vitro*. **A,** DU145 DIAPH3-depleted overexpressing (OE) emerin display reduced migration in comparison with DIAPH3-depleted cells, quantified using a Boyden chamber assay. **B,** Representative immunoblot showing levels of emerin and β-actin in DU145 control, DIAPH3-depleted cells or DIAPH3-depleted emerin overexpressing cells. **C,** Reduction of p-ERK in DU145 DIAPH3-depleted emerin overexpressing cells. Representative immunoblot showing levels of emerin, p-ERK, ERK and β-actin are shown. **D,** Representative images of DU145 control or emerin-depleted cells. DNA (Hoechst, blue) and lamin A (FITC, green) staining are shown (scale bar 10 μm). Emerin-depleted cells exhibit disrupted nuclear shape. **E,** Representative images of BT-549 control or emerin-depleted cells. DNA (Hoechst, blue) and lamin A (FITC, green) staining are shown (scale bar 10 μm). Arrows indicate nuclear blebs or cytosolic vesicles. **F,** Representative images of DU145 control or emerin-depleted stained with the lipid affinity dye CellMask Orange. Arrows point to nuclear blebs. **G,** Quantification of nuclear circularity in DU145 control and emerin-depleted cells (perfect circle=1; <1 represents departure from circularity). **H,** DU145 emerin-depleted cells show increased filtration of cells compared to controls, as measured by PMF, indicating

increased cell deformability. **I,** DU145 emerin-depleted cells shed EV containing DNA. **J,** DU145 emerin-depleted cells display enhanced migration and **K,** invasion quantified using a Boyden chamber assay. Graphs show mean ± s.d. **P<0.01, ***P<0.001. Unpaired t-test. **L,** Quantification of colonies in DU145 control or emerin-depleted cells by ImageJ.

Figure 3. Loss of emerin promotes metastasis *in vivo*. **A,** Luciferase activity at weeks 3, 4 and 5 after intracardiac cancer cell injection, (n=8 mice for DU145 control and n=7 for DU145 emerin-depleted). **B,** Graphs representing the number of organs affected by metastatic lesions identified in each mouse. Graph show mean ± s.d. **P<0.01, Unpaired t-test. **C,** Representative H&E and cytokeratin IHC staining of the brain, lungs, adrenal glands, liver (scale bar 50 μm) and bones (scale bar 300 μm) from the mice injected with DU145 emerin-depleted cells.

Figure 4. Lamin A/C downregulation is frequent in metastatic prostate cancer and lamin A/C-depletion leads to nuclear shape instability. **A,** Waterfall plot displays *LMNA* gene expression in 260 cases of metastatic castration resistance prostate cancer (36). **B,** Boxplot showing relative lamin A/C mRNA expression levels in PCS1-3 subgroups (36) (PCS1, n=377; PCS2, n=428; PCS3, n=516). PCS1 is the most aggressive of the 3 subtypes. **C,** Kaplan-Meier curves show differential rate of biochemical recurrence (BCR) between LMNA high and low group of prostate cancer patients from the TCGA cohort (n=550). The media value of LMNA expression was used to divide patients into high and low groups. **D,** Lamin A/C-depleted cells exhibit nuclear shape instability. Representative images of DU145 control or lamin A/C-depleted cells. DNA (Hoechst,

blue) and emerin (FITC, green) staining are shown (scale bar 10 μm). Enlarged merged image of cells displaying nuclear envelope blebbing. **E,** Quantification of nuclear circularity in DU145 control or lamin A/C-depleted cells (perfect circle=1; <1 represents departure from circularity). **F,** DU145 lamin A/C-depleted cells shed EV containing DNA. **G,** DU145 lamin A/C-depleted cells display enhanced migration and **H,** invasion using quantified using a Boyden chamber assay. Graphs show mean ± s.d. **P<0.01, ***P<0.001. Unpaired t-test. **I,** Representative images of metastatic lesions of mice injected with DU145 lamin A/C-depleted cells. Metastatic tumors were immunostained with an anti-emerin antibody. Arrows point to emerin-positive nuclear envelope blebs, emerin mislocalization and EV-like structures in the metastatic tissues (scale bar 50 μm).

Figure 5. Emerin is a marker of nuclear shape instability in prostate cancer. **A,** Detection of emerin-positive particles in prostate cancer. Immunofluorescent staining was performed for emerin, histone H3 (HH3, nuclear mask), and cytokeratin 18 (epithelial mask) on a prostate cancer TMA (n=80). In normal prostate epithelium, emerin is localized to the nuclear envelope (Top Row, white arrows). In cancer prostate epithelium, distinct emerin-positive particles are visible (red arrows). Scale bar 100 μm. **B-E,** Quantitative analysis of emerin-positive particles in human prostate cancer. **B,** The number of emerin-positive particles was quantified in tumor and adjacent benign prostate tissue. Pairwise analysis **C,** and ratio **D,** of particles in tumor and adjacent benign tissue; note an elevation of particles in tumor tissue. **E,** The ratio of emerin-positive particles correlates with BCR. **F,** Peripheral blood specimens from prostate patients were tested for CTCs. The CTCs DAPI-positive/cytokeratin (CK)-positive/CD45-negative were stained

with emerin. Membrane staining (FITC-cholera toxin B, green) was additionally used to identify CTCs with membrane blebs that were emerin-positive (middle panel DAPI-positive/cytokeratin-positive/cholera toxin B). **G,** Emerin intensity in CTCs were compared with WBC in the same high-power fields from the same patients (>50 fields were analyzed); $P < 0.001$). **H,** Emerin-positive particles identified in CTCs.

Reis-Sobreiro et al. Fig.1

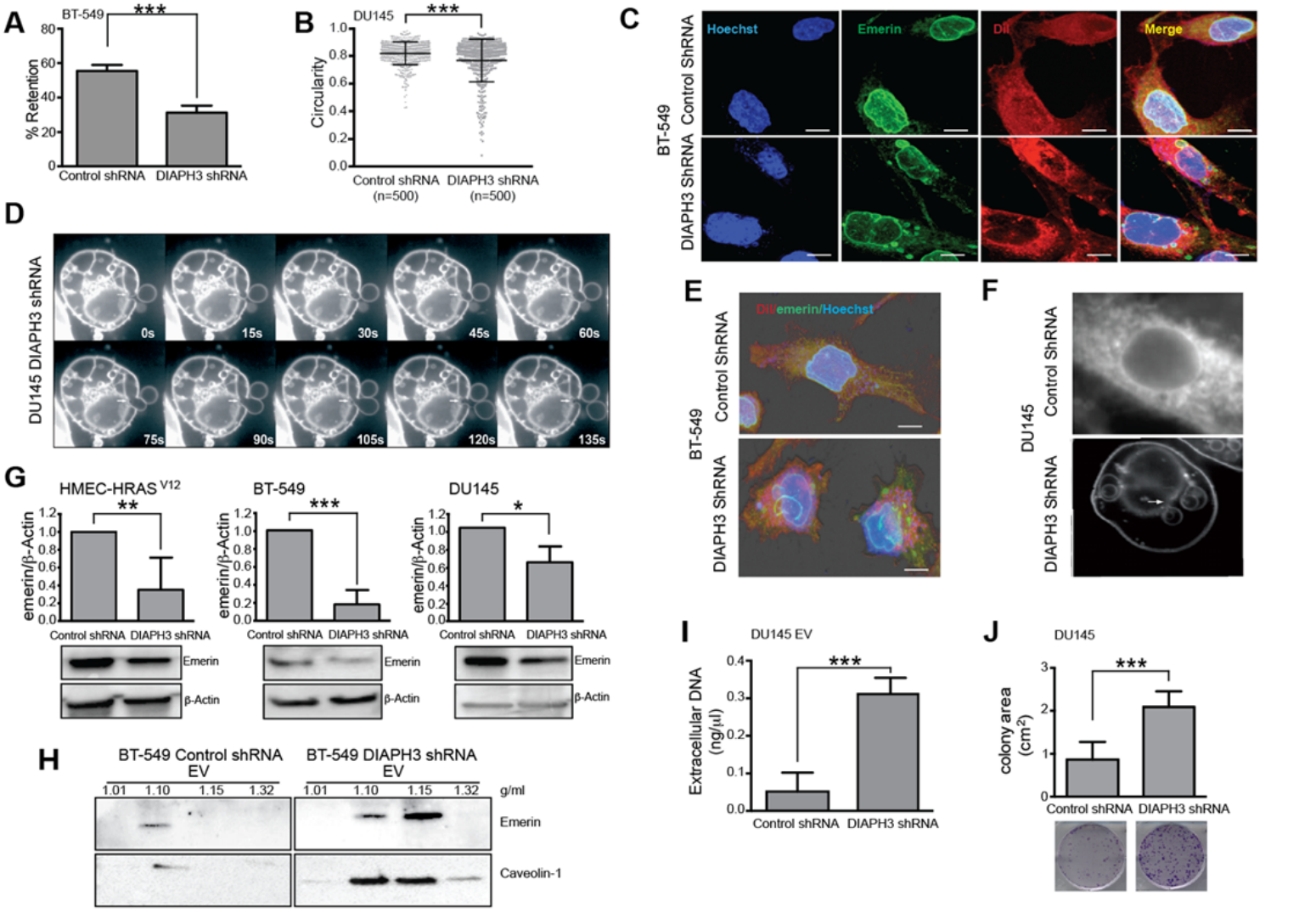

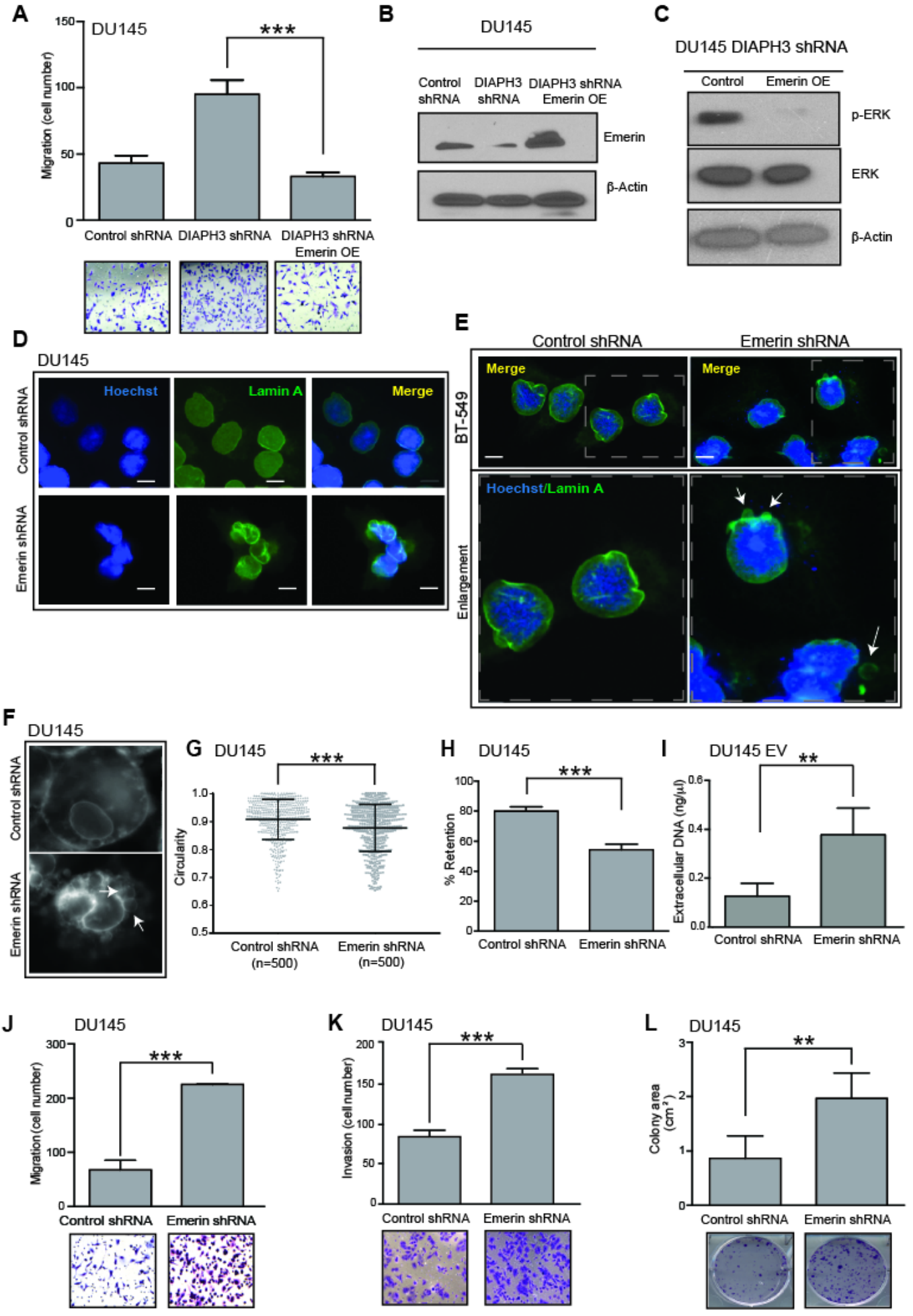

Reis-Sobreiro et al. Fig.3

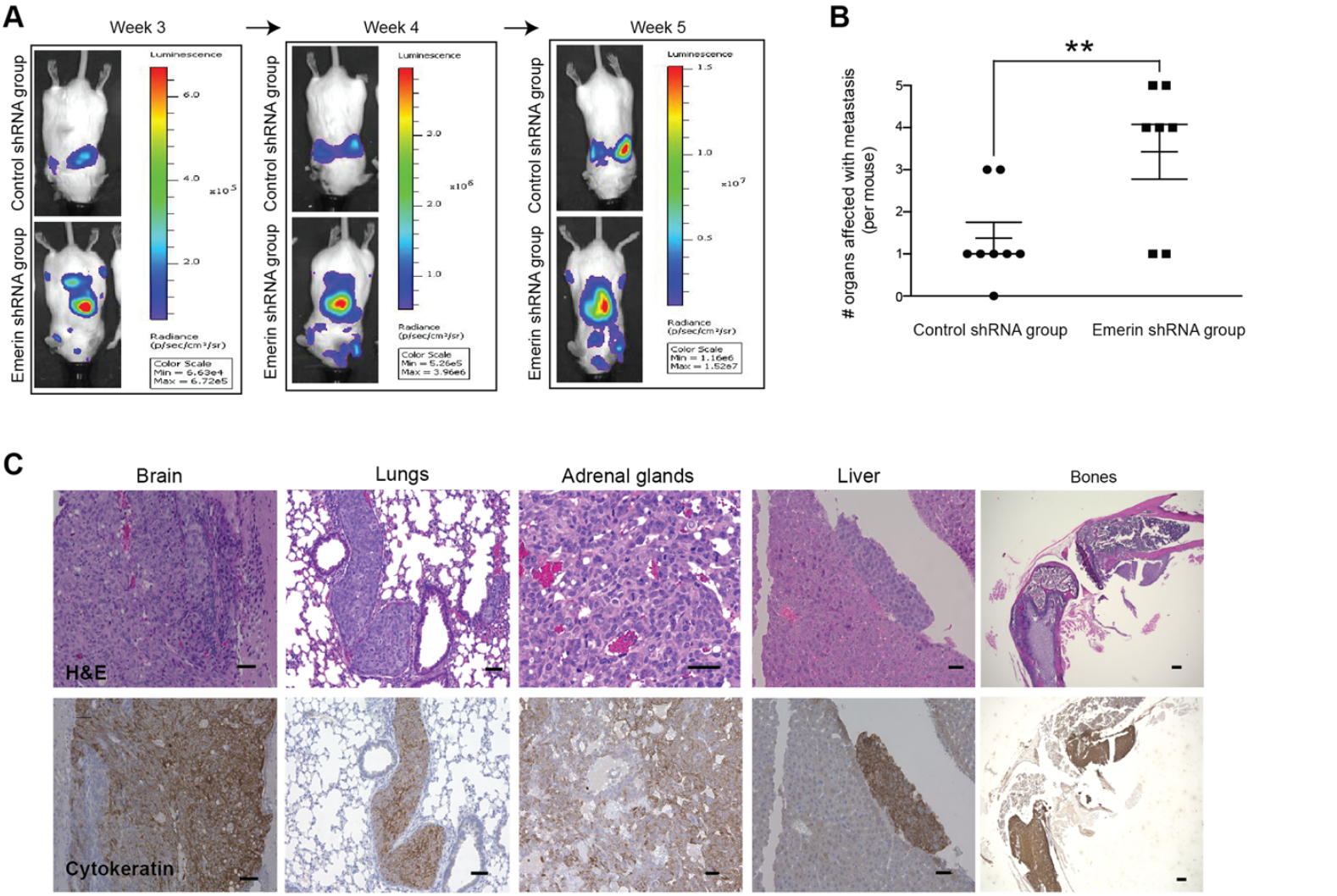

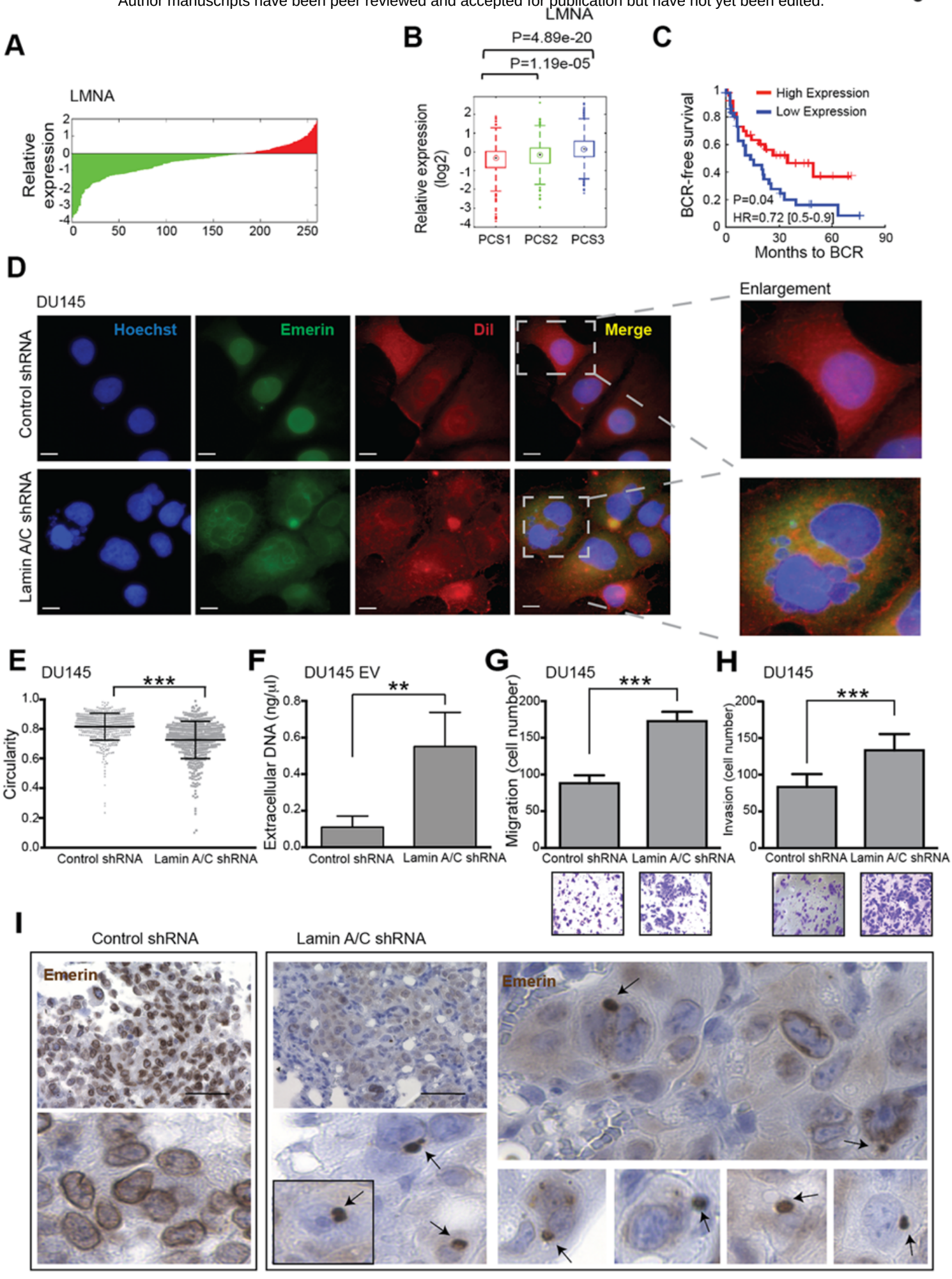

Reis-Sobreiro et al. Fig.5

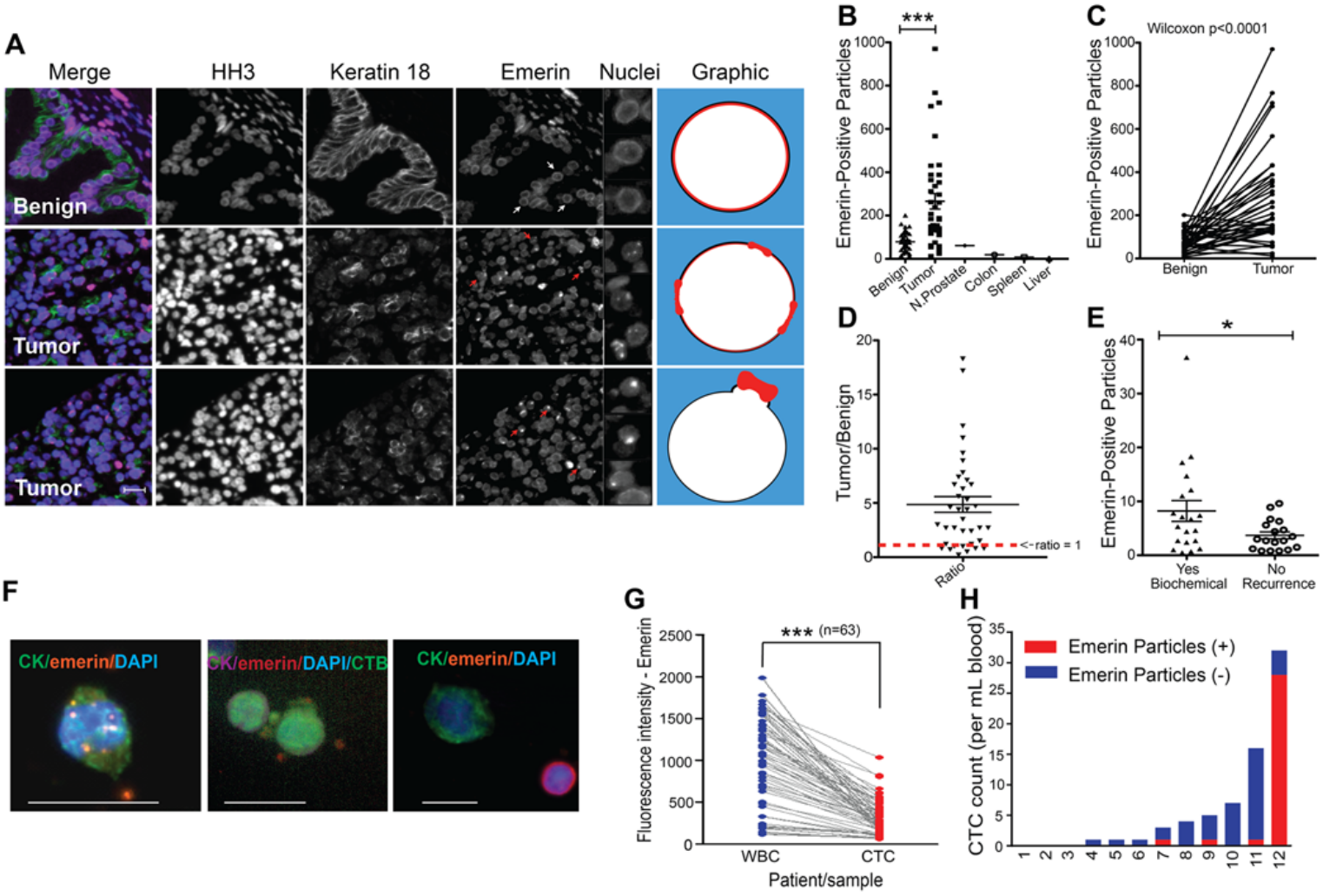

Cancer Research
The Journal of Cancer Research (1916–1930) | The American Journal of Cancer (1931–1940)

AACR American Association for Cancer Research

Emerin deregulation links nuclear shape instability to metastatic potential

Mariana Reis-Sobreiro, Jie-Fu Chen, Tatiana Novitskaya, et al.

Cancer Res Published OnlineFirst August 28, 2018.